



# VLBI images at 327 MHz of compact steep spectrum and GHz-peaked spectrum sources from the 3C and PW samples

D. Dallacasa,<sup>1,2★</sup> M. Orienti,<sup>2★</sup> C. Fanti<sup>2</sup> and R. Fanti<sup>2</sup>

<sup>1</sup>*Dipartimento di Fisica e Astronomia, Università di Bologna, via Gobetti 93/2, I-40129, Bologna, Italy*

<sup>2</sup>*INAF – Istituto di Radioastronomia, via Gobetti 101, I-40129, Bologna, Italy*

Accepted 2021 April 8. Received 2021 April 8; in original form 2021 January 11

## ABSTRACT

We present results on global very long baseline interferometry (VLBI) observations at 327 MHz of 18 compact steep-spectrum (CSS) and GHz-peaked spectrum (GPS) radio sources from the 3C and the Peacock & Wall catalogues. About 80 per cent of the sources have a ‘double/triple’ structure. The radio emission at 327 MHz is dominated by steep-spectrum extended structures, while compact regions become predominant at higher frequencies. As a consequence, we could unambiguously detect the core region only in three sources, likely due to self-absorption affecting its emission at this low frequency. Despite their low surface brightness, lobes store the majority of the source energy budget, whose correct estimate is a key ingredient in tackling the radio source evolution. Low-frequency VLBI observations able to disentangle the lobe emission from that of other regions are therefore the best way to infer the energetics of these objects. Dynamical ages estimated from energy budget arguments provide values between  $2 \times 10^3$  and  $5 \times 10^4$  yr, in agreement with the radiative ages estimated from the fit of the integrated synchrotron spectrum, further supporting the youth of these objects. A discrepancy between radiative and dynamical ages is observed in a few sources where the integrated spectrum is dominated by hotspots. In this case the radiative age likely represents the time spent by the particles in these regions, rather than the source age.

**Key words:** galaxies: active – galaxies: nuclei – quasars: general – radio continuum: general.

## 1 INTRODUCTION

Powerful radio sources hosted in elliptical galaxies and quasars represent about 10 per cent of the population of active galactic nuclei. Although their linear sizes span several orders of magnitude, from a few parsecs up to several Mpc, the radio morphology is described by the same ingredients: a central core, where the relativistic plasma is produced and accelerated; two bipolar jets that channel the plasma towards the outermost regions; the hotspots that mark the place where the jet impacts with the external medium; and the lobes where particles are deposited after being further accelerated in the hotspot, and where eventually they age. As a consequence of the dominant mechanism (i.e. acceleration/cooling), the spectral shape of the various components is different. For example the core is characterized by a flat or inverted spectrum, indicating the presence of synchrotron self-absorption, and more properly should be defined as the region where the jet becomes optically thick at a given frequency. The spectrum of the hotspots is usually a power law with spectral index  $\alpha \sim 0.5\text{--}0.7$  ( $S_\nu \propto \nu^{-\alpha}$ ) marking the presence of high Mach number shock-induced particle acceleration, while the lobes have a steep spectrum with  $\alpha > 0.7$ , indicating significant energy losses.

Flux-limited catalogues selected at low frequencies, like the 3CRR (Laing, Riley & Longair 1983), are dominated by steep-spectrum radio sources, usually hosted in galaxies, whose radio emission mainly arises from the lobes. On the other hand, in

catalogues selected at high frequencies, like the Peacock & Wall (Peacock & Wall 1981) and the Australia Telescope 20-GHz Survey (AT20G Murphy et al. 2010), we expect a larger fraction of sources with bright and compact cores typically with a flat spectrum, and usually associated with quasars. Interestingly, in both low- and high-frequency selected catalogues about 10–15 per cent of the sources are unresolved on arcsecond scales. Statistical studies showed that the majority of these objects are intrinsically compact with linear sizes  $< 20$  kpc, and not foreshortened by projection effects (Fanti et al. 1990). When observed with adequate spatial resolution they usually show a two-sided radio structure resembling a scaled-down version of Fanaroff–Riley radio sources. Depending on their linear size (LS) they are termed compact symmetric objects (CSO,  $LS < 1$  kpc) or medium-sized symmetric objects (MSO,  $1 \text{ kpc} < LS < 20$  kpc). The main characteristic of CSO/MSO sources is the steep synchrotron radio spectrum that turns over at frequencies between  $\sim 50$  MHz and a few GHz. Depending on the peak frequency  $\nu_p$ , these compact objects are termed compact steep-spectrum (CSS;  $\nu_p < 500$  MHz) and gigahertz-peaked spectrum (GPS;  $\nu_p > 500$  MHz) radio sources (O’Dea 1998). CSS/GPS sources are optically identified with both galaxies and quasars, the latter being more commonly found among high-frequency peaking GPS sources (e.g. Tornaiainen et al. 2007).

Many studies were carried out to understand the nature of CSS/GPS sources, i.e. whether they are small because in an early stage of their evolution (e.g. Fanti et al. 1995), or frustrated by an extraordinary dense environment (e.g. van Breugel, Miley & Heckman 1984). Estimates of kinematic and radiative ages of a few thousand years (Polatidis & Conway 2003; Murgia 2003; Gugliucci

★ E-mail: ddallaca@ira.inaf.it (DD); orienti@ira.inaf.it (MO)



**Table 1.** Antennas participating the observations. Column 1: observing date; Column 2: observing mode; Column 3: antennas.

Date	Obs. mode	Antennas
04-11-1992	MkII	Wb, Jb, Nt, Tr, Sm, Gb, Pt, La, Nl, Br, Ov, Hn, VLA
20-02-1995	MkIII	Wb, Jb, Nt, Gb, Pt, La, Nl, Br, Hn, Kp, Mk, Fd, Sc

*Note.* Wb, Westerbork; Jb, Jodrell Bank; Nt, Noto; Tr, Torun; Sm, Simeiz (Crimea); Gb, 43-m Green Bank telescope; Pt, Pie Town; La, Los Alamos; Nl, North Liberty; Br, Brewster; Ov, Owens Valley; Hn, Hancock; VLA, Very Large Array – single antenna; Kp, Kitt Peak; Mk, Mauna Kea; Fd, Fort Davis; Sc, St. Croix.

et al. 2005; Giroletti & Polatidis 2009; An et al. 2012a), together with the lack of any evidence of uncommonly rich ambient medium (e.g. Fanti et al. 2000; Siemiginowska et al. 2005), strongly support the genuine youth of these objects. However, in some sources there is evidence of jet-medium interaction that may temporarily frustrate the source expansion (e.g. Labiano et al. 2006; Dallacasa et al. 2013; Morganti et al. 2013; Sobolewska et al. 2019; Zovaro et al. 2019). Detailed information on GPS/CSS sources can be found in the review by O’Dea & Saikia (2021).

Evolutionary models have been proposed to trace the various stages of the source growth (e.g. Fanti et al. 1995; Readhead et al. 1996; Alexander 2000; Snellen et al. 2000; An & Baan 2012b) and to determine how the physical parameters evolve. The main ingredient at the basis of the source evolution is the balance between the jet power and the ram pressure on the external medium. Therefore, a correct estimate of the jet thrust and the energetics of the radio source is fundamental for drawing a clear picture of the source evolution.

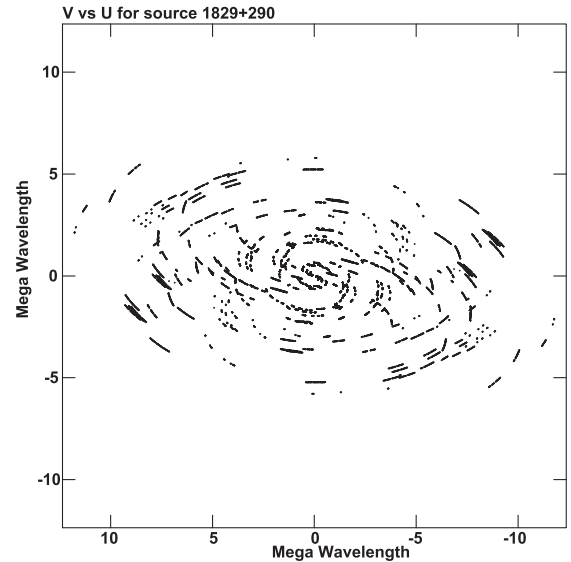
In this paper, we present results of global very long baseline interferometry (VLBI) observations at 327 MHz of 18 CSS/GPS objects from the 3C and Peacock & Wall catalogues. Our aim is the characterization of the radio morphology at low frequency and the estimate of the energetics and dynamical age of the radio sources. To achieve this goal we need observations at low frequency to detect the steep-spectrum emission from the lobes, where the majority of energy is stored, and with high spatial resolution to disentangle the lobe emission from that of other regions. For CSS/GPS have compact linear size, only low-frequency global VLBI observations can fulfil the requirements. So far only a handful of works based on VLBI images at 327 MHz are available. They mainly focus on variable extragalactic sources (Altschuler et al. 1995; Chuprikov et al. 1999; Rampadarath, Garrett & Polatidis 2009) or on deep wide field VLBI survey (Lenc et al. 2008). The data presented here are the deepest and with the highest angular resolution at 327 MHz for a sample of CSS/GPS published so far.

This paper is organized as follows. In Section 2, we describe the radio observations and data reduction; results are reported in Section 3 and discussed in Section 4. A brief summary is presented in Section 5.

Throughout this paper, we assume  $H_0 = 71 \text{ km s}^{-1} \text{ Mpc}^{-1}$ ,  $\Omega_M = 0.27$ ,  $\Omega_\Lambda = 0.73$ , in a flat Universe. The spectral index is defined as  $S(\nu) \propto \nu^{-\alpha}$ .

## 2 OBSERVATIONS AND DATA REDUCTION

The observations presented in this paper were obtained with VLBI networks at 327 MHz in different observing modes (MkII and MkIII) on 1992 November 4 and 1995 February 20. Antennas involved in the observing runs are listed in Table 1. Observations were carried out in snapshot mode in single polarization with a total bandwidth of 2 and 14 MHz for MkII and MkIII, respectively. Correlation was

**Figure 1.**  $(u, v)$  coverage of the VLBI network at 327 MHz in units of wavelengths for the source 1829 + 290.

performed at the Caltech-JPL VLBI Correlator. A priori amplitude calibration was made using the system temperature measurements and the antenna gains for each telescope. The uncertainty on the flux density scale is approximately 10 percent. The target sources and the calibrators were fringe-fitted with a solution interval of 60 s. The coherent time at this frequency is rather short ( $\sim 10$  s). Therefore, the 2-s integration data underwent a number of self-calibration iteration before time averaging. Editing, fringe-fitting, and all the usual operations on VLBI data sets were performed using the Astronomical Image Processing System (AIPS) software. Final images were produced after a few imaging and phase-only self-calibration iterations. The final noise on the image plane is typically between 1.5 and 5 mJy beam $^{-1}$ . In Fig. 1, we show the  $(u, v)$  coverage for the source 1829 + 290 as an example. We note that the lack of baselines shorter than 0.1 M $\lambda$  prevents the detection of regions larger than  $\sim 2$  arcsec, i.e. comparable to the lobe emission detected by MERLIN observations in a few sources (see Section 3).

## 3 RESULTS

All the sources are clearly detected in our 327-MHz VLBI observations. The flux density and the angular size of each component are measured, using the task JMFIT in AIPS that performs a Gaussian fit to the source components on the image plane. In a few sources, multiple components were fitted simultaneously and the residuals were inspected in order to be sure that no additional components were necessary. In the case of diffuse emission that cannot be fitted



by a Gaussian profile, the flux density was derived using TVSTAT in AIPS that allows the selection of a polygonal region on the image plane. In this case, the angular size was measured on the contour image and corresponds to roughly twice the size of the full width at half-maximum (FWHM) of a conventional Gaussian, covering a similar area (Readhead 1994).

Often the flux density that is recovered by our VLBI images is only a fraction of the emission obtained from observations with lower resolution at the same frequency. Such missing flux density may be due to additional emission from lobes on large scales that could not be fully sampled by our VLBI observations (Table 2).

Observational parameters of each source component are reported in Table 3, whereas VLBI images at 327 MHz are presented in Figs 2–19. On each image, we provide the source name, the peak flux density (mJy beam<sup>-1</sup>) and the first contour (f.c.) intensity (mJy beam<sup>-1</sup>), which is three times the off-source noise level. Contour levels increase by a factor of 2. The restoring beam is plotted on the bottom left-hand corner.

### 3.1 Low-frequency radio structure

The structure of all the 18 sources is resolved. Seven sources have a double morphology, seven have a triple structure (although the central component is not always associated with the core, on the basis of the steepness of the spectrum), while the remaining four have a complex morphology. In six sources, we could disentangle the emission of at least one of the lobes from the hotspot contribution, crucial information for estimate the dynamical age of the radio source (see Section 4). In 11 sources, the flux density recovered from our observations is  $\leq 80$  per cent of that measured in low-resolution observations at the same frequency. This missing flux is likely caused by the lack of short baselines and poor ( $u, v$ ) coverage that make our observations unsuitable for detecting arcsecod-scale diffuse emission.

The core component is detected in three sources (3C 138, 3C 298, and 0223 + 341), while in 3C 318 it is tentatively associated with the central region. The small percentage of core detection may be explained by either synchrotron self-absorption of the component at such a low frequency, or a blending of the source core and emission from other steep-spectrum components that cannot be resolved by the angular resolution of our observations.

Significant flux density ratio ( $R > 2$ ) between the two sides of the radio sources is found for 10 out of the 14 sources with double/triple morphology (Fig. 20). The largest values ( $R > 8$ ) are found in quasars, and may be ascribed to beaming effects. In general, galaxies have low flux density ratios, with the exception of 0404 + 768, which is among the smallest of our sample. This is in agreement with what was found by Orienti (2016), where the smaller sources are also those with the higher flux density ratios. The other galaxy with high flux density ratio is 1829 + 290. However, in this source we are considering two internal components, rather than the lobes which extend more than one arcsec away from the central region and are not imaged by our observations. If we consider their flux density from MERLIN observations, we end up with  $R \sim 1$  and an LLS of about 20 kpc (Spencer et al. 1989), consistent with the fact that asymmetries get less important as the source grows.

### 3.2 Spectral indices

We complemented our 327 MHz VLBI observations with information from the literature in order to have a more complete description of the source structure and spectral information. In many cases,

high-resolution data exist in the literature to allow the analysis of the component spectra from 327 MHz up to 22 GHz.

In Table 3, we give a low frequency spectral index ( $\alpha_l$ ), usually computed between 0.327 and 0.610 (or 1.7) GHz, and a high frequency spectral index ( $\alpha_h$ ), computed in a range that depends on the available data and on the spectral shape (see notes to Table 3). Unless mentioned otherwise, the 610 MHz data used for computing the spectral index are from Nan et al. (1991a), those at 1.7 and 5 GHz are from Dallacasa et al. (1995), Lüdke et al. (1998), and Dallacasa et al. (2013), while those at 8.4, 15, and 22 GHz are from Mantovani et al. (2013).

Uncertainty in the spectral index may be large depending on the component structure: compact regions have small spectral index errors ( $\pm 0.1$ , mainly from the amplitude calibration uncertainty), while extended low-surface brightness components may result artificially steeper/flatter due to missing flux density caused by the lack of short spacing at the various frequencies (see Section 3.3). When there is no secure identification of the same component at different frequencies, we do not provide any value for the spectral index in Table 3.

We computed the average high frequency spectral index ( $\langle \alpha_h \rangle$ ), the average low frequency spectral index ( $\langle \alpha_l \rangle$ ), and their standard deviation for the central components and for the lobes (inclusive of hotspot emission which cannot be disentangled). For the former, we find the following:

$$\begin{aligned} \text{(i)} \quad \langle \alpha_h \rangle &= 0.7 \pm 0.1, \sigma = 0.2, \\ \text{(ii)} \quad \langle \alpha_l \rangle &= 0.1 \pm 0.1, \sigma = 0.4, \end{aligned}$$

while for the latter we have

$$\begin{aligned} \text{(i)} \quad \langle \alpha_h \rangle &= 1.2 \pm 0.1, \sigma = 0.4, \\ \text{(ii)} \quad \langle \alpha_l \rangle &= 0.6 \pm 0.1, \sigma = 0.4. \end{aligned}$$

As expected the spectra of the central components are flatter than those of the lobes/hotspots. The change of the spectral shape below  $\sim 1$  GHz may be due to either a low-frequency turnover caused by synchrotron self-absorption, or the presence of a spectral break at higher frequencies caused by the source age. About 70 per cent of the sources have a peak frequency of the integrated spectrum  $\nu_p \geq 100$  MHz, implying a moderate/significant dimming of the flux density at 327 MHz due to opacity (Table 2). On the other hand, for 90 per cent of the objects the spectral break estimated by Murgia et al. (1999) is at a frequency below the highest one used to compute  $\alpha_h$ , supporting the steepening produced by radiative losses.

### 3.3 Notes on individual sources

Here, we provide a brief description of the sources studied in this paper. For sources with a two-sided structure, we provide the flux density ratio which is computed between the emission from the whole component (i.e. lobe + hotspot) on each side, unless stated otherwise. When we have the information on the core position we computed the arm-length ratio between the lobes.

#### CSS sources from the 3C sample

##### 3.3.1 3C 43 [ $Q$ , $z = 1.459$ ]

In our VLBI image at 327 MHz 3C 43 shows a distorted structure where the radio emission comes mainly from the western region which is resolved into several sub-components with a knotty arc-shaped structure (components from A to G in Fig. 2). Component A marks the position of the source core that is clearly visible in VLBI images at higher frequencies (Fanti et al. 2002), but



**Table 2.** CSS/GPS sources from the 3C and PW samples. Column 1: source name; Column 2: optical identification: G = galaxy, Q = quasar; Column 3: redshift; Column 4: peak frequency from Fanti et al. (1990); Column 5: total flux density at 327 MHz from the VLBI data presented in this paper (fraction of flux density that is recovered in VLBI images); Column 6: total flux density at 327 MHz from observations with low spatial resolution; Columns 7 and 8: largest angular size and largest linear size derived from VLBI images presented in this paper; Column 9: reference for the low-resolution flux density. 1: Jeyakumar et al. (2000), 2: WENSS (Rengelink et al. 1997), 3: Kühr et al. (1981), 4: Douglas et al. (1996). Column 10: source morphology as derived from our VLBI images at 327 MHz. C = complex morphology, D = double structure, T = triple structure.

Source	Id	z	$\nu_p$ (MHz)	$S_{\text{VLBI}}^{92 \text{ cm}}$ Jy (per cent)	$S_{\text{tot}}^{92 \text{ cm}}$ (Jy)	LAS (arcsec)	LLS (kpc)	Ref.	Morph.
(1)	(2)	(3)	(4)	(5)	(6)	(7)	(8)	(9)	(10)
3C 43	Q	1.459	<20	5.1 (60)	8.4	1.24	10.57	1	C
3C 49	G	0.621	120	7.4 (97)	7.6	1.00	6.78	1	D
3C 93.1	G	0.243	60	2.2 (30)	7.5	0.17	0.64	2	C
3C 119	G	1.023	150	17.9 (100)	17.7	0.42	3.39	2	C
3C 138	Q	0.759	100	19.3 (97)	19.8	0.62	4.57	1	T
3C 237	G	0.877	50	17.1 (98)	17.4 <sup>a</sup>	1.21	9.4	3	D
3C 241	G	1.617	40	5.9 (78)	7.6	0.83	7.10	1	D
3C 298	Q	1.437	80	20.1 (61)	32.9	1.49	12.69	1	T
3C 318	Q	1.574	<40	5.5 (60)	9.2 <sup>a</sup>	1.11	9.50	4	T
3C 343	Q	0.988	250	12.8 (95)	13.6	0.40	0.32	2	C
3C 343.1	G	0.75	250	11.7 (87)	13.5	0.35	2.57	2	D
0223 + 341	Q	2.91	250	2.2 (60)	3.7	0.82	6.47	2	T
0316 + 161	G	0.907	900	5.9 (79)	7.5 <sup>a</sup>	0.40	3.13	3	D
0404 + 768	G	0.5985	600	8.9 (96)	9.3	0.130	0.87	2	D
1153 + 317	Q	0.417	100	5.4 (65)	8.2	0.90	4.93	2	T
1819 + 396	G	0.798	100	5.8 (82)	7.0	0.80	6.01	2	D
1829 + 290	G	0.842	100	3.8 (69)	5.5	0.38	2.93	2	T
2342 + 821	Q	0.735	400	4.4 (79)	5.6	0.17	1.24	2	T

<sup>a</sup>The low resolution flux density refers to observations at 365 MHz.

it is partially absorbed at 327 MHz. Only a hint of the eastern component is detected, while the northern component, imaged at 1.7 GHz with MERLIN observations (Fanti et al. 2002), is resolved out.

### 3.3.2 3C 49 [G, $z = 0.621$ ]

In our VLBI image at 327 MHz 3C 49 shows an asymmetric double structure (Fig. 3) with compact hotspots at each end. The spectrum of the eastern lobe is steep, while the spectral index of the western component is initially flat and slowly steepens above 610 MHz (Table 3). This suggests that the radio emission of this component is dominated by a compact hotspot, which

is likely self-absorbed at low frequencies. The source core, detected at high frequencies (Fanti et al. 1989; Sanghera et al. 1995; van Breugel et al. 1992; Lüdke et al. 1998), is not detected in our observation, and should be considered self-absorbed. The flux density ratio at 327 MHz is  $S_W / S_E = 1.4$ , but increases with frequency owing to the different spectral indices of the two components.

The arm-length ratio is derived from the 5-GHz MERLIN image (Lüdke et al. 1998), where the source core is clearly detected, and is  $R_R = 0.4$ , where the brighter component is the closer to the core.

### 3.3.3 3C 93.1 [G, $z = 0.243$ ]

3C 93.1 has an amorphous radio structure and no compact region is found in the VLBI image at 327 MHz (Fig. 4). The spectral index computed between 327 MHz and 1.7 GHz from Spencer et al. (1989) is flat with  $\alpha = 0.0$ , but this may be caused by the severe flux density loss in our VLBI data.

### 3.3.4 3C 119 [G, $z = 1.023$ ]

In our VLBI image at 327 MHz (Fig. 5), 3C 119 shows a compact component, Ce, slightly elongated towards south and surrounded by diffuse emission, in agreement with data at 610 MHz (Nan et al. 1991a). The spectral index computed between 327 and 610 MHz is rather flat, suggesting the presence of unresolved compact components where self-absorption becomes important, whereas it steepens at higher frequencies (Table 3).

### 3.3.5 3C 138 [Q, $z = 0.759$ ]

The radio source 3C 138 shows an asymmetric triple structure (Fig. 6). The eastern component, E, extending for about 390 mas (2.87 kpc) from the centre, is the brightest one and is interpreted as the approaching jet (Fanti et al. 1989). Component E1 marks the hotspot. The western component, W, is interpreted as the source counter-lobe, and is located at  $\sim 230$  mas (1.7 kpc) from the centre and extends for 440 mas (3.3 kpc) in the NS direction.

The spectral indices of the extended components and of the hotspot E1, all relatively flat at low frequencies, steepen above 610 MHz (Table 3). The central component, C, has instead an absorbed spectrum, suggesting that it hosts the source core. The flux density ratio at 327 MHz between the eastern and western components is  $S_E / S_W \sim 8$ , while the arm-length ratio is  $R_R = 1.7$ .

### 3.3.6 3C 237 [G, $z = 0.877$ ]

The radio source 3C 237 shows a double morphology in our VLBI image at 327 MHz (Fig. 7). The eastern component, E, is resolved in the EW direction, while the western component, W, is elongated



**Table 3.** Component parameters. Column 1: source name; Column 2: source component; Column 3: VLBI flux density at 327 MHz; Columns 4 and 5: major and minor axis; Column 6: position angle of the major axis; Column 7: spectral index between 327 and 610 MHz, if not stated otherwise; Column 8: high-frequency spectral index. See the notes for the frequency pairs.

Source	Comp.	$S_{327}$ (Jy)	$\theta_{\text{maj}}$ (mas)	$\theta_{\text{min}}$ (mas)	pa (deg)	$\alpha_l$	$\alpha_h$
(1)	(2)	(3)	(4)	(5)	(6)	(7)	(8)
3C 43	A + B	$0.72 \pm 0.07$	$47 \pm 1$	$12 \pm 1$	$167 \pm 2$	1.3	–
	C	$1.15 \pm 0.11$	$58 \pm 1$	$20 \pm 1$	$166 \pm 1$	0.3	–
	D	$1.38 \pm 0.14$	$26 \pm 1$	$20 \pm 1$	$94 \pm 2$	0.4	$0.6^c e$
	E + F	$1.05 \pm 0.10$	$102 \pm 2$	$28 \pm 1$	$90 \pm 1$	1.0	–
	G	$0.36 \pm 0.04$	$157 \pm 6$	$91 \pm 4$	$40 \pm 5$	2.7	–
3C 49	W <sup>a</sup>	$0.39 \pm 0.04$	370	200	65	–	–
	E	$0.91 \pm 0.09$	$79 \pm 2$	$52 \pm 2$	$45 \pm 2$	1.1	$1.1^c g$
	E <sup>a</sup>	$3.07 \pm 0.31$	800	460	80	$1.2^b$	$1.4^d g$
	W	$3.22 \pm 0.03$	$31 \pm 1$	$28 \pm 1$	$13 \pm 1$	0.0	$1.5^d e$
	W <sup>a</sup>	$4.31 \pm 0.43$	420	290	90	$0.5^b$	$0.9^d g$
3C 93.1	Total <sup>a</sup>	$2.18 \pm 0.22$	170	120	10	–	–
3C 119	E	$10.12 \pm 1.01$	$130 \pm 1$	$97 \pm 1$	$52 \pm 1$	0.0	–
	Ce	$5.61 \pm 0.56$	<52	–	–	$0.0^b$	$0.8^d e$
	W	$2.23 \pm 0.22$	$137 \pm 1$	$51 \pm 1$	$17 \pm 1$	–	–
	Total	–	–	–	–	$0.6^k$	$1.9^f, h$
3C 138	E1	$6.64 \pm 0.66$	$72 \pm 1$	$51 \pm 1$	$17 \pm 1$	0.0	$1.5^c e$
	E <sup>a</sup>	$16.00 \pm 1.60$	400	340	60	0.5	$0.8^d h$
	C	$1.32 \pm 0.13$	$58 \pm 1$	$42 \pm 1$	$8 \pm 2$	-0.3	$0.6^c e$
	W <sup>a</sup>	$1.99 \pm 0.20$	420	260	175	0.2	$1.5^c e$
3C 237	E <sup>a</sup>	$6.55 \pm 0.66$	400	350	90	$0.7^b$	$1.3^d g$
	W <sup>a</sup>	$10.56 \pm 1.06$	560	420	–	$0.7^b$	$1.2^d g$
3C 241	E	$3.40 \pm 0.34$	$64 \pm 1$	$45 \pm 1$	$104 \pm 1$	0.7	$1.8^d g$
	W2	$0.70 \pm 0.07$	$76 \pm 1$	$38 \pm 1$	$66 \pm 2$	0.5	$1.2^c g$
	W1	$1.80 \pm 0.18$	$63 \pm 1$	$44 \pm 1$	$118 \pm 1$	0.3	$1.2^c g$
3C 298	E	$5.98 \pm 0.60$	$187 \pm 2$	$156 \pm 1$	$50 \pm 1$	$1.4^b$	$1.4^c e$
	E <sup>a</sup>	$8.55 \pm 0.85$	900	520	120	$0.7^b$	$1.3^d h$
	J	$0.72 \pm 0.07$	$48 \pm 1$	$12 \pm 3$	$107 \pm 1$	-1.3	$1.0^c h$
	C	$0.11 \pm 0.01$	–	–	–	$-0.6^b$	$0.5^d h$
	W	$4.93 \pm 0.49$	$99 \pm 1$	$71 \pm 1$	$27 \pm 1$	$0.5^c$	$1.1^d h$
	W <sup>a</sup>	$10.73 \pm 1.07$	680	420	0	–	–
3C 318	N	$0.33 \pm 0.03$	$82 \pm 2$	$57 \pm 2$	$25 \pm 3$	$0.2^b$	–
	Ce <sup>a</sup>	$2.10 \pm 0.21$	360	160	30	0.0	$0.8^d g$
	S1 <sup>a</sup>	$1.19 \pm 0.12$	330	200	20	$0.9^b$	–
	S2 <sup>a</sup>	$1.93 \pm 0.19$	330	220	120	–	–
	S1 + S2	–	–	–	–	0.2	$1.4^d h$
3C 343	Total <sup>a</sup>	$12.78 \pm 1.28$	360	180	125	0.4	$1.0^d h$
3C 343.1	E <sup>a</sup>	$3.73 \pm 0.37$	230	180	120	0.2	$1.0^c h$
	W <sup>a</sup>	$7.96 \pm 0.80$	300	260	–	0.4	$1.1^c h$
0223 + 341	N	$0.04 \pm 0.01$	$75 \pm 2$	$20 \pm 2$	$80 \pm 1$	–	–
	C	$0.98 \pm 0.10$	$45 \pm 2$	$25 \pm 2$	$70 \pm 1$	$-0.6^b$	$0.6^d h$
	S1	$0.08 \pm 0.01$	$70 \pm 2$	$50 \pm 2$	$16 \pm 2$	1.0	$1.0^c g$
	S	$0.44 \pm 0.04$	$70 \pm 2$	$60 \pm 1$	$72 \pm 2$	1.1	$1.1^c f$
	S <sup>a</sup>	$1.15 \pm 0.11$	880	380	170	1.1	$1.1^c h$
0316 + 161	N	$2.70 \pm 0.27$	$35 \pm 1$	$22 \pm 1$	$139 \pm 2$	$-0.5^b$	$1.3^d g$
	S <sup>a</sup>	$3.19 \pm 0.32$	320	180	140	$1.2^b$	$2.4^d e$
0404 + 768	E	$1.28 \pm 0.13$	$54 \pm 1$	$43 \pm 1$	$7 \pm 2$	$0.7^b$	$0.9^d e$
	W	$7.54 \pm 0.75$	$36 \pm 1$	$31 \pm 1$	$41 \pm 1$	$0.3^b$	$0.5^d e$
1153 + 317	N	$1.47 \pm 0.15$	$43 \pm 1$	$33 \pm 1$	$44 \pm 2$	$0.3^b$	$1.1^d g$
	Ce	$0.03 \pm 0.01$	–	–	–	$0.5^b$	$0.5^c g$
	S	$2.16 \pm 0.22$	$34 \pm 2$	$24 \pm 2$	$145 \pm 1$	–	–
	S <sup>a</sup>	$3.95 \pm 0.40$	410	140	150	$0.5^b$	$1.1^d g$
	N <sup>a</sup>	$1.55 \pm 0.16$	240	190	100	$0.8^b$	$1.4^d g$
1819 + 396	S <sup>a</sup>	$4.24 \pm 0.42$	370	220	130	$0.4^b$	$1.1^d g$
	W <sup>a</sup>	$0.45 \pm 0.04$	180	150	40	–	–
1829 + 290	Ce	$0.03 \pm 0.01$	–	–	–	–	–
	E	$2.93 \pm 0.29$	$54 \pm 1$	$24 \pm 1$	$90 \pm 2$	–	–
	E <sup>a</sup>	$3.27 \pm 0.32$	260	170	180	$0.2^b$	$1.2^e h$
	W	$3.32 \pm 0.33$	$21 \pm 2$	$18 \pm 2$	$42 \pm 1$	–	–
2342 + 821	W <sup>a</sup>	$3.71 \pm 0.37$	100	90	150	$0.2^b$	$0.8^d e$



Table 3 – continued

Source	Comp.	$S_{327}$ (Jy)	$\theta_{\text{maj}}$ (mas)	$\theta_{\text{min}}$ (mas)	pa (deg)	$\alpha_l$	$\alpha_h$
(1)	(2)	(3)	(4)	(5)	(6)	(7)	(8)
	Ce	$0.31 \pm 0.03$	$20 \pm 2$	$12 \pm 1$	$103 \pm 1$	$0.4^b$	$1.0^{d,e}$
	E	$0.35 \pm 0.04$	$60 \pm 2$	$15 \pm 1$	$129 \pm 1$	$0.9^b$	$1.0^{d,e}$

<sup>a</sup>The flux density was derived by TVSTAT in AIPS. The component angular size was measured on the contour image and is roughly twice the FWHM of a conventional Gaussian covering a similar area. <sup>b</sup>Spectral index computed between 327 MHz and 1.7 GHz. Two letters indicate other frequency pairs: <sup>c</sup> = 0.610, <sup>d</sup> = 1.7 GHz, <sup>e</sup> = 5 GHz, <sup>f</sup> = 8.4 GHz, <sup>g</sup> = 15 GHz, <sup>h</sup> = 22 GHz, <sup>k</sup>  $\alpha_{0.327}^{8.4}$ .

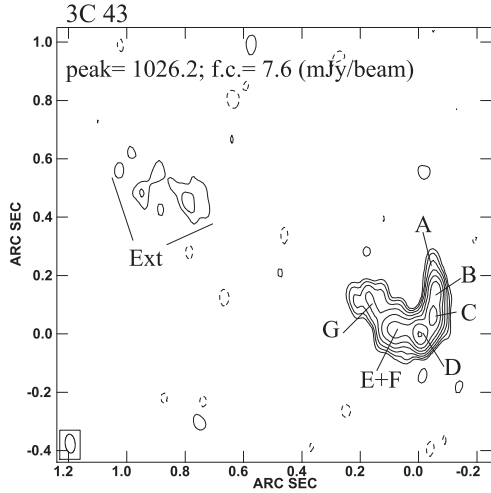


Figure 2. VLBI image at 327 MHz of 3C 43.

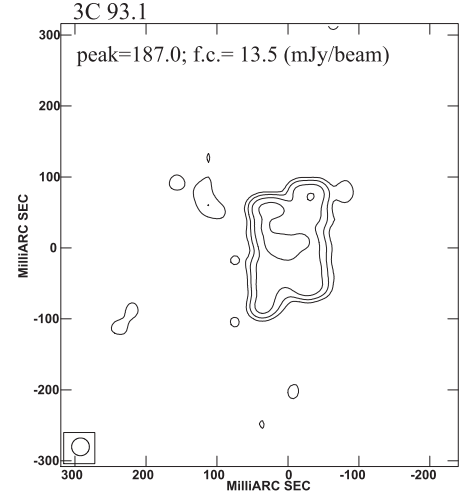


Figure 4. VLBI image at 327 MHz of 3C 93.1.

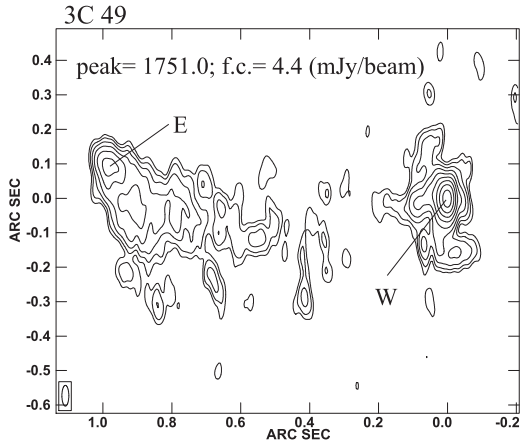


Figure 3. VLBI image at 327 MHz of 3C 49.

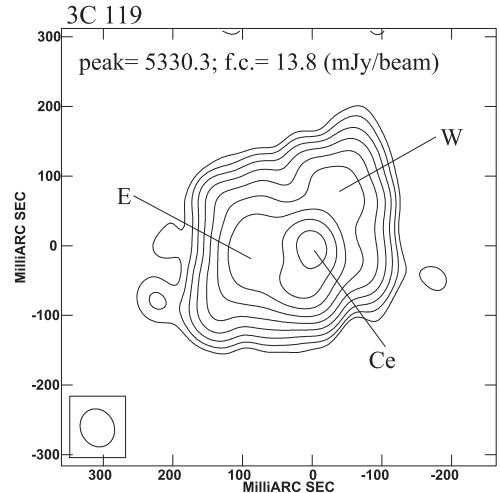


Figure 5. VLBI image at 327 MHz of 3C 119.

towards south, in agreement with what was found in previous works at different frequencies (e.g. Fanti et al. 1986; Nan et al. 1991a; Lüdke et al. 1998). The lobes look edge-brightened, but no obvious hotspot has been clearly detected at any frequency in the literature. The spectra of both lobes E and W have a similar shape, showing a flattening from high to low frequencies. The flux density ratio at 327 MHz between the western and eastern component is  $S_W/S_E \sim 1.6$ , which remains roughly constant at higher frequencies (Lüdke et al. 1998), while the arm-length ratio, measured on the 5-GHz image where the core is detected, is  $R_R = 1.5$ .

### 3.3.7 3C 241 [*G*, $z = 1.617$ ]

The radio source 3C 241 shows a double structure in our VLBI image at 327 MHz (Fig. 8). The western component is resolved into two compact regions, W1 and W2, separated by 120 mas (1.0 kpc) and aligned with the weak flat-spectrum source core detected by MERLIN observations at 5 GHz (Sanghera et al. 1995) and at 15 GHz (van Breugel et al. 1992). The spectra of components W1 and W2 are very similar, slightly flat at low frequencies followed by a steepening



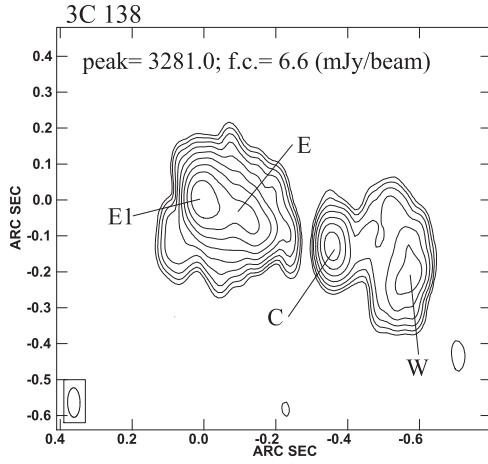


Figure 6. VLBI image at 327 MHz of 3C 138.

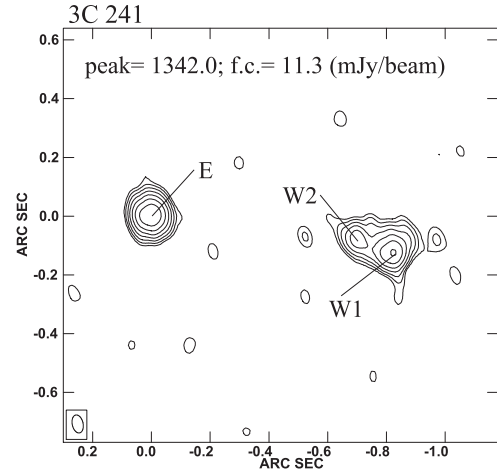


Figure 8. VLBI image at 327 MHz of 3C 241.

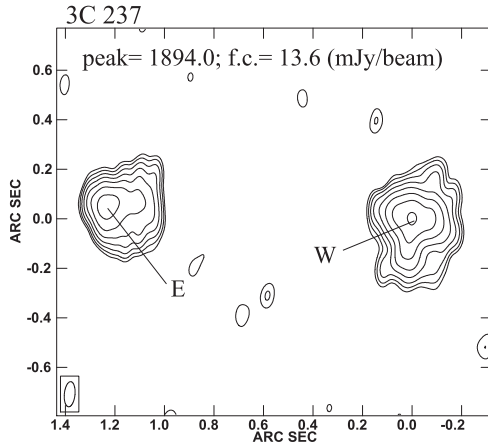


Figure 7. VLBI image at 327 MHz of 3C 237.

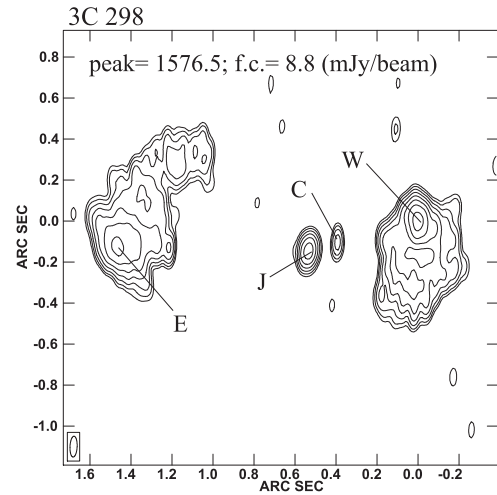


Figure 9. VLBI image at 327 MHz of 3C 298.

with the same slope above 610 MHz. The eastern lobe has a steeper spectrum at both low and high frequencies (Table 3). The flux density ratio at 327 MHz between the eastern (E) and western (W1 + W2) component is  $S_E/S_W \sim 2.3$ . Owing to its flatter spectrum above 610 MHz, the western component becomes the brighter at 5 GHz with  $S_W/S_E \sim 2.2$  (Lüdke et al. 1998). Following our assumption that the arm-length ratio is below unity in case of a brighter-when-closer asymmetry, we have that  $R_R = 1.4$  at 327 MHz, while it switches to 0.7 at 5 GHz (Fig. 21).

### 3.3.8 3C 298 [*Q*, $z = 1.437$ ]

In our VLBI image at 327 MHz, 3C 298 shows an S-shaped structure dominated by the emission from the two lobes extending clockwise with respect to the embedded compact hotspots (Fig. 9). Hotspots are clearly detected and their distance from the core is about 930 mas (7.9 kpc) and 560 mas (4.8 kpc) for the eastern and western hotspots, respectively. A low frequency turnover is visible for the western lobe, likely caused by the embedded self-absorbed component W. Component E, instead, has a straight spectrum over the entire frequency range (Table 3). Two compact components, J and C, are located between the lobes. They have inverted spectra at frequencies below 610 MHz, and steepen at higher frequencies (Table 3). VLBI

images at 1.7 and 5 GHz presented by Fanti et al. (2002) show that J is a compact knot, while C is the core. The flux density ratio between the western and eastern component is  $S_W/S_E = 1.2$  at 327 MHz, and increases to 1.8 at 5 GHz (Fanti et al. 2002). The arm-length ratio is  $R_R = 0.4$ , where the western component is the closer to the core.

### 3.3.9 3C 318 [*Q*, $z = 1.574$ ]

In our VLBI image at 327 MHz (Fig. 10), 3C 318 shows an asymmetric triple structure, where the central component, labelled C, likely hosts the weak source core and is located at about 0.6 arcsec (5.0 kpc) and 0.4 arcsec (3.5 kpc) far from the northern and southern components, respectively. A one-sided jet, characterized by a bright knot, emerges from the north-eastern part of the core region. The spectral index at low frequencies of N, C, and S1 + S2 is relatively flat (Table 3), but this may be caused by the significant flux density loss of our VLBI data. The flux density ratio at 327 MHz between the southern (S1+S2) and northern component is  $S_S/S_N \sim 9.7$ .



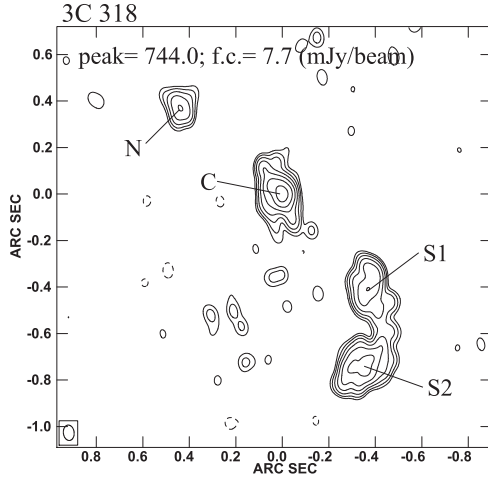


Figure 10. VLBI image at 327 MHz of 3C 318.

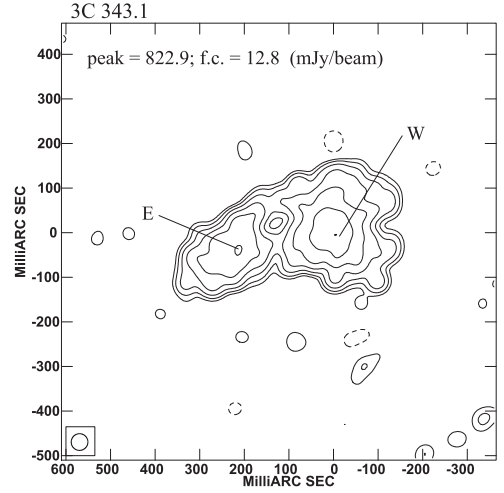


Figure 12. VLBI image at 327 MHz of 3C 343.1.

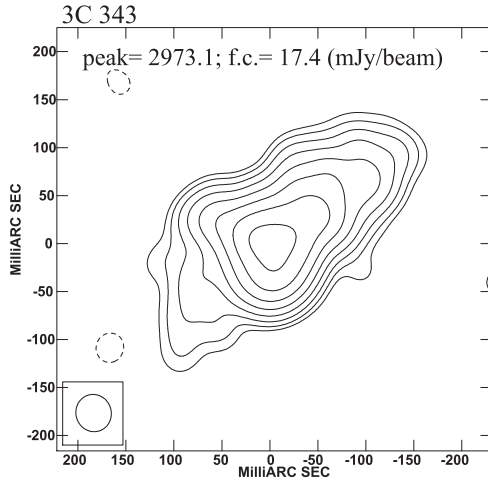


Figure 11. VLBI image at 327 MHz of 3C 343.

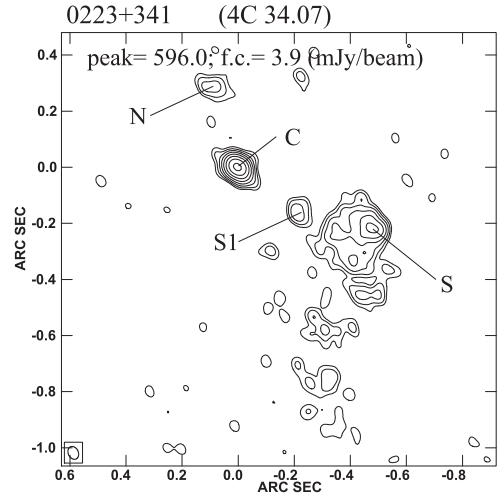


Figure 13. VLBI image at 327 MHz of 0223 + 341 (4C 34.07).

### 3.3.10 3C 343 [*Q*, $z = 0.988$ ]

In our VLBI image at 327 MHz (Fig. 11), 3C 343 is elongated in the north-west direction, in agreement with the structure found by Nan et al. (1991a) at 610 MHz and by Lüdke et al. (1998) in 5-GHz MERLIN data. The spectrum of the whole source increasingly steepens with increasing frequencies (Table 3).

### 3.3.11 3C 343.1 [*G*, $z = 0.75$ ]

In our VLBI image at 327 MHz (Fig. 12), 3C 343.1 is resolved into two asymmetric lobes separated by about 215 mas (1.6 kpc). Component W is slightly elongated in the EW direction, while component E has a position angle of about  $125^\circ$ . The core has been found neither in our image nor in the literature. The spectra of the two components are similar: initially quite flat, they steepen above 610 MHz (Table 3). The flux density ratio at 327 and 610 MHz is  $S_W/S_E \sim 2$ .

### CSS and GPS sources from the PW sample

### 3.3.12 0223 + 341 [*Q*, $z = 2.91$ ]

At 327 MHz, 0223 + 341 (alias 4C 34.07) displays a complex structure dominated by a bright compact component, labelled C in Fig. 13, which is located between two extended features, labelled N and S. Another bright compact structure, labelled S1 in Fig. 13 is located at about 0.27 arcsec (2.1 kpc) from component C in the direction of the southern lobe. The southern component terminates to the west with a compact feature, possibly a hotspot. The extended emission present South of component S is clearly visible in VLA images at lower resolution (Lenc et al. 2008), but it is almost totally resolved out in our VLBI image. The presence of the northern lobe, detected in deep 327-MHz VLBI data (Lenc et al. 2008), suggests that component C is likely hosting the source core, as also proposed by Lenc et al. (2008), but also see Mantovani et al. (2013) for a different interpretation. The flux density ratio at 327 MHz between component N and S is  $S_S/S_N = 17$ , while the arm-length ratio is  $R_R = 1.7$  if we assume that component C is the source core.



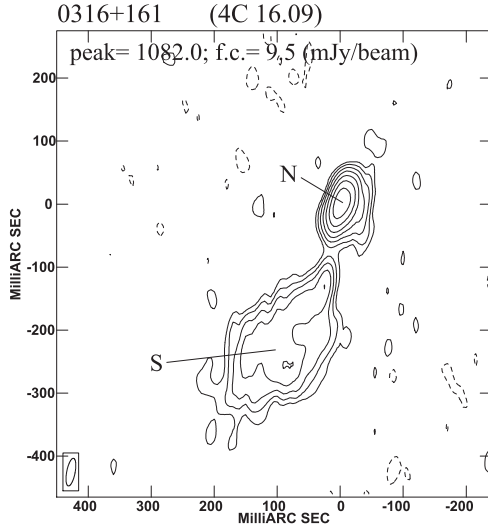


**Figure 14.** VLBI image at 327 MHz of 0316 + 161 (4C 16.09).

### 3.3.13 0316 + 161 [ $G$ , $z = 0.907$ ]

At 327 MHz the radio emission of 0316 + 161 (alias 4C 16.09) is dominated by a bright elongated component, labelled N in Fig. 14, from which a diffuse low-surface brightness structure emerges and extends for about 300 mas (2.3 kpc) to the South. In our image the core would be located roughly at the northern tip of the extended structure, labelled S in Fig. 14. The northern component has initially an inverted spectrum which then switches its trend and steepens, while the southern component has a steep spectrum. The flux density ratio at 327 MHz between the southern and northern component is  $S_S/S_N = 1.1$ . Owing to its flat spectrum, the northern component becomes the brighter at high frequency with  $S_N/S_S = 14$  at 1.7 GHz (Dallacasa et al. 2013). Following our assumption that the arm-length ratio is below unity in case of a brighter-when-closer asymmetry, we have that  $R_R = 1.7$  at 327 MHz, while it switches to 0.6 at 1.7 GHz (Fig. 21).

### 3.3.14 0404 + 768 [ $G$ , $z = 0.5985$ ]

At 327 MHz 0404 + 768 (alias 4C 76.03) shows an asymmetric double structure (Fig. 15). In images at higher resolution (Dallacasa et al. 1995, 2013) the core is clearly visible and is characterized by an inverted spectrum. The western lobe has a rather flat, almost straight spectrum from 327 MHz to 8.4 GHz, while the spectrum of the eastern component is steeper (Table 3). The flux density ratio between the western and eastern component is  $S_W/S_E = 5.9$  at 327 MHz. It becomes 9.5 and 7.0 at 1.7 and 5 GHz, respectively (Dallacasa et al. 2013), owing to the different slope of the spectra. The arm-length ratio derived from the VLBI image at 5 GHz is  $R_R \sim 0.6$ , with the brighter component being the closer to the core.

### 3.3.15 1153 + 317 [ $Q$ , $z = 0.417$ ]

In our VLBI image at 327 MHz, 1153 + 317 (alias 4C 31.38) shows a very asymmetric double structure with a weak, possibly compact, component in between (labelled Ce in Fig. 16). The northern lobe, labelled N, is slightly resolved, while the southern lobe, labelled S, is characterized by a bright and compact region, visible only at 327 MHz, that is possibly a hotspot aligned with components Ce

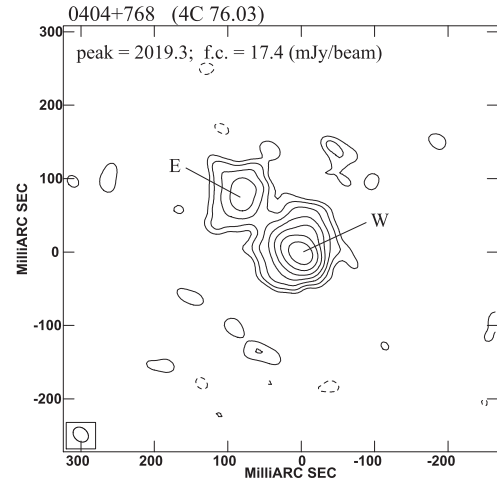


**Figure 15.** VLBI image at 327 MHz of 0404 + 768 (4C 76.03).

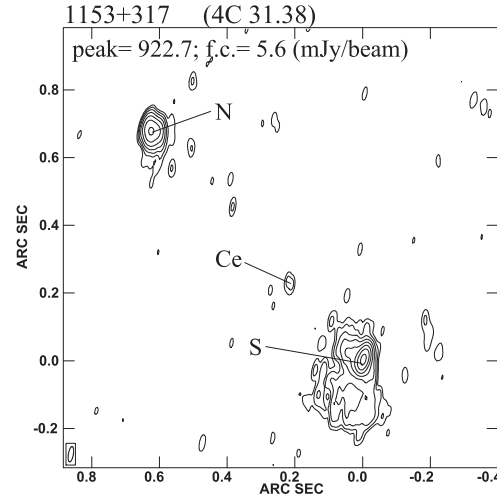


**Figure 16.** VLBI image at 327 MHz of 1153 + 317 (4C 31.38).

and N. Diffuse emission flows from the hotspot to the south. The spectral information is not adequate to unambiguously classify Ce component as the source core. The spectra of the two lobes, quite flat at low frequencies, steepen above 1.7 GHz (Table 3). The flux density ratio at 327 MHz is  $S_S/S_N = 2.7$ , becoming smaller ( $S_S/S_N = 2$ ) at higher frequencies (Spencer et al. 1989), as the contribution of the diffuse emission of the southern component gets less important.

### 3.3.16 1819 + 396 [ $G$ , $z = 0.798$ ]

In our VLBI image at 327 MHz (Fig. 17), 1819 + 396 (alias 4C 39.56) has a double morphology which extends for about 0.7 arcsec (5.3 kpc). The radio emission is dominated by the southern component, S, whose structure resembles a curved jet. The spectra of both lobes have a break above 1.7 GHz, the southern component being the flatter at low frequencies (Table 3). The flux density ratio between component S and N is  $S_S/S_N = 2.6$ .



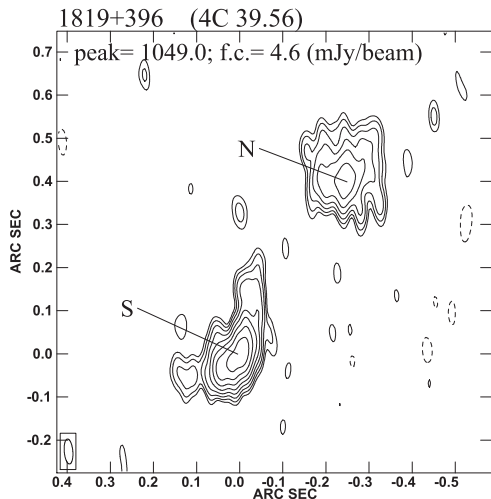


Figure 17. VLBI image at 327 MHz of 1819 + 396 (4C 39.56).

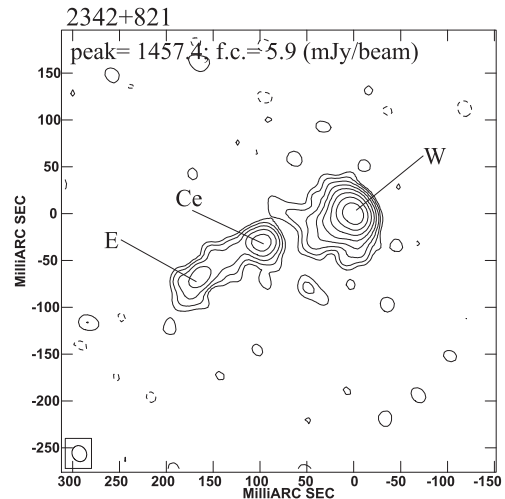


Figure 19. VLBI image at 327 MHz of 2342 + 821.

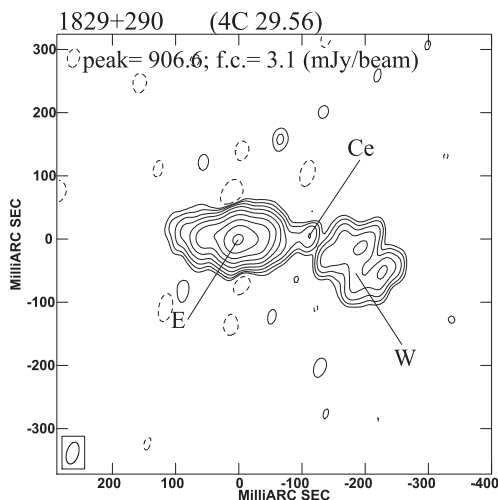


Figure 18. VLBI image at 327 MHz of 1829 + 290 (4C 29.56).

### 3.3.17 1829 + 290 [*G*, *z* = 0.842]

In our VLBI image at 327 MHz of 1829 + 290 (alias 4C 29.56), only the central component, labelled E, is detected, while the faint lobes, visible in MERLIN images (Spencer et al. 1989), are not detected (Fig. 18). In addition we observe a central component, Ce, and a weak western component, W, undetected in previous VLBI observations at 1.7 GHz (Dallacasa et al. 1995), which is roughly oriented in the same direction of the southern lobe. Component Ce does not seem to have any counterpart at 1.7 GHz. The radio spectrum of component E is initially quite flat, and then curves slowly, becoming straight and steep above 5 GHz. The flux density ratio between components E and W is  $S_E/S_W = 7.3$  at 327 MHz.

### 3.3.18 2342 + 821 [*Q*, *z* = 0.735]

In our VLBI image at 327 MHz, 2342 + 821 displays a triple well-aligned radio structure with a bright component to the west that dominates the radio emission (Fig. 19). A jet-like feature is present in the south-east direction. The initial spectra of components W and

Ce are rather flat, and both steepen above 1.7 GHz. Component E, instead, has an approximately straight steep spectrum. No evidence of the source core has been found. The flux density ratio between component W and E is  $S_W/S_E = 9.5$ .

## 4 DISCUSSION

Diffuse low-surface brightness regions are difficult to observe in VLBI observations at centimetre wavelengths due to their steep spectra and large angular scale. These features mark the place where reside the oldest electron populations that radiate at low frequencies as a consequence of the severe energy losses they experienced during their lifetime. This is particularly true for compact lobes, like those of CSS/GPS sources, where the magnetic field is substantially stronger than that in the lobes of classical Fanaroff-Riley radio galaxies (e.g. Fanti et al. 1995; Croston et al. 2005).

Our low-frequency observations are usually dominated by low-surface brightness diffuse emission, whereas compact components, like hotspots and cores, become predominant at higher frequencies. This is reflected in the analysis of the flux density and arm-length asymmetry. For the eight sources with an unambiguous core detection either in our images or in the literature, we find that among the four with  $R > 2$  (i.e. a significant asymmetry in flux density) in only one of them the brighter component is the closer to the core. This low fraction is in contrast with the much higher percentage ( $\sim 50$  percent) that is found at higher frequencies (Dallacasa et al. 2013). However, if we consider the flux density ratio at higher frequencies also for our target sources, the situation changes and the percentage of sources with a brighter-when-closer behaviour increases to 50 percent (Fig. 21). This is caused by the different spectral index of the source components that makes lobe dominate at low frequencies, while they are overwhelmed by the emission from hotspots at high frequencies.

Although the surface brightness of lobes is generally lower than that in cores, jets and hotspots, these extended structures store a large fraction of the source energy budget.

Given their large volumes, the total energy derived for lobes (under minimum energy condition (Pacholczyk 1970); see the Appendix) is at least one order of magnitude larger than that derived for the hotspots (Table 4).



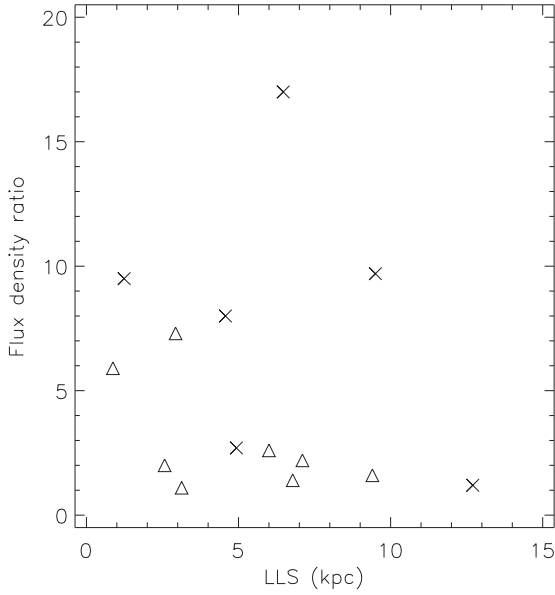


**Figure 20.** Flux density ratio versus largest linear size (LLS) for the 14 sources with a double/triple morphology. Crosses are quasars, while triangles are galaxies.

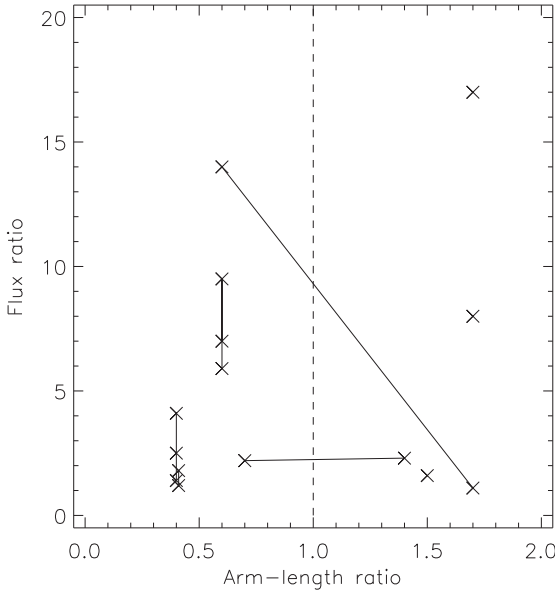


**Figure 21.** Flux density ratio versus arm-length ratio for the eight CSS/GPS sources with a core detection. The vertical dashed line corresponds to an arm-length ratio of unity. Values below the unity indicates that the brighter component is the closer to the core. When the flux density could be measured at various frequencies, points are connected with a line. A change in the arm-length ratio for the same source indicates that the brighter component at low frequency becomes the fainter at high frequency.

**Table 4.** Physical parameters for the hotspots and lobes.

	Hotspots	Lobes
$L$ (erg s <sup>-1</sup> )	$5 \times 10^{43}$ – $3 \times 10^{45}$	$10^{44}$ – $6 \times 10^{45}$
$E_{\min}$ (erg)	$10^{56}$ – $10^{58}$	$10^{57}$ – $6 \times 10^{59}$
$u_{\min}$ (erg cm <sup>-3</sup> )	$4 \times 10^{-8}$ – $10^{-6}$	$10^{-9}$ – $3 \times 10^{-7}$
$p_{\text{eq}}$ (dyne cm <sup>-2</sup> )	$3 \times 10^{-8}$ – $6 \times 10^{-7}$	$2 \times 10^{-10}$ – $2 \times 10^{-7}$
$H_{\text{eq}}$ (mG)	0.3–1.5	0.1–0.8

**Table 5.** Source ages and magnetic fields. Column 1: source name; column 2: source component; column 3: dynamical age; column 4: equipartition magnetic field of the lobe; columns 5 and 6: radiative ages and equipartition magnetic field from Murgia et al. (1999).

Source	comp.	$\tau_{\text{dyn}}$ 10 <sup>4</sup> yr	$H_{\text{eq, lobe}}$ mG	$\tau_{\text{rad}}$ 10 <sup>4</sup> yr	$H_{\text{eq}}$ mG
3C 49	W	2.4	0.2	0.1	7.0
	E	3.6	0.2	0.1	7.0
3C 138	E	3.0	0.4	1.7	1.0
3C 298	W	4.8	0.4	>5	1.6
	E	3.3	0.2	>5	1.6
1153 + 317	S	0.9	0.4	0.5	1.7
2342 + 821	W	0.2	0.5	≤0.13	4.5

For the sources where it is possible to disentangle the hotspot contribution from the lobe emission, we estimate the source age following energy budget arguments. The dynamical source age is estimated by

$$\tau_{\text{dyn}} \sim 2 \times E_{\min}/F_e, \quad (1)$$

where  $E_{\min}$  is the total energy stored in the lobe,  $F_e$  is the jet energy flux, and the factor of 2 accounts for the work spent in inflating the lobe (Fanti et al. 2002). The jet energy flux is  $F_e = c\Pi$ , where  $\Pi$ , the jet thrust, corresponds to  $\Pi = p_{\text{eq}} \times A$ , with  $p_{\text{eq}}$  is the pressure in the hotspot and  $A$  is the impact area. We obtain dynamical ages between  $2 \times 10^3$  and  $5 \times 10^4$  yr (Table 5). The values derived in this way should be representative of the order of magnitude of the dynamical ages, owing to the strong assumptions on the minimum energy condition, a constant jet thrust during the source lifetime, and the large uncertainty on the volume. On the other hand, the missing flux density should not influence the estimate more than a factor of 1.3. These values are in agreement with the radiative ages derived by Murgia et al. (1999) by fitting the integrated radio spectrum, with some exceptions. However, if we compare the equipartition magnetic field that we estimate in the lobes and the one assumed by Murgia et al. (1999) we see that the latter is much higher in a few sources, and is more similar to the one we estimate in the hotspots. A remarkable example is 3C 49, where  $\tau_{\text{dyn}}$  and  $\tau_{\text{rad}}$  differ more than an order of magnitude. Assuming their  $\tau_{\text{rad}}$ , Murgia et al. (1999) estimated that 3C 49 is expanding at a superluminal velocity ( $v > 4c$ ), which is unlikely for a radio source, hosted by a galaxy, whose radio emission should not be affected by beaming effects. If we compute  $\tau_{\text{rad}}$ , assuming the magnetic field in the lobes we obtain  $\tau_{\text{rad}} \sim 4 \times 10^4$  yr, which is similar to  $\tau_{\text{dyn}}$ , while the velocity expansion becomes about  $0.3c$ , consistent with what is found by kinematic studies of CSO sources (e.g. Giroletti & Polatidis 2009).

## 5 SUMMARY

We presented VLBI images at 327 MHz of 18 CSS/GPS radio sources from the 3C and Peacock & Wall catalogues. The conclusions that we can draw from this investigation are as follows:

- All the sources are clearly detected and imaged. About 80 percent of the sources have a ‘double/triple’ morphology, and the source core is detected in only 16 percent of them. This is likely the consequence of self-absorption that is severe at the observing frequency.
- For the 8 sources with information on the core position, either from these data or from literature, we studied the asymmetries in flux density and arm-length. Half of the sources have a roughly symmetry



in flux density between the two sides of the radio emission. Only in one out of the four asymmetric sources, the brighter component is the closer to the core. The situation changes if we consider flux density ratio at higher frequencies, where the emission is dominated by compact hotspot components with a flatter spectrum than the lobes.

(iii) The dynamical ages derived on energy budget arguments are between  $2 \times 10^3$  and  $5 \times 10^4$  yr, in rough agreement with the radiative ages estimated by the analysis of the integrated radio spectrum. The larger discrepancy between radiative and dynamical ages are found in sources where the integrated spectrum and the magnetic field are dominated by the hotspot components. In this case, the radiative age likely represents the time spent by the particles in these regions rather than the genuine age of the source.

A comprehensive study of the physics of extragalactic radio sources requires information covering a large part of the radio spectrum: high frequencies for picking up the region of fresh particle injection and acceleration, and low frequencies to infer the energetics of the radio source. The combination of future facilities, like next-generation very large array, and LOFAR with the addition of the international baselines, will be pivotal for population studies of CSS/GPS sources.

## ACKNOWLEDGEMENTS

We thank the anonymous referee for reading the manuscript carefully and making valuable suggestions. We thank the European VLBI Network and the United States VLBI Network for carrying out the observations. The WSRT is operated by the Netherlands Foundation for Research in Astronomy with the financial support of the Netherlands Organization for Scientific Research (NWO). The National Radio Astronomy Observatory is operated by Associated Universities, Inc., under contract with the National Science Foundation. This research has made use of the NASA/IPAC Extragalactic Database (NED), which is operated by the Jet Propulsion Laboratory, California Institute of Technology, under contract with the National Aeronautics and Space Administration. DD still acknowledges the Commission of the European Union for the award of a Fellowship, although it happened a long ago. The authors thanks A. Medici and Z. Cai for help in the data reduction. The WENSS project was a collaboration between the Netherlands Foundation for Research in Astronomy and the Leiden Observatory. The WENSS team consisted of Ger de Bruyn, Yuan Tang, Roeland Rengelink, George Miley, Huub Röttgering, Malcolm Bremer, Martin Bremer, Wim Brouw, Ernst Raimond, and David Fullagar.

## DATA AVAILABILITY

Final images are available upon reasonable request.

## REFERENCES

Alexander A., 2000, *MNRAS*, 319, 8  
 Altschuler D. R., Gurvits L. I., Alef W., Dennison B., Graham D., Trotter A. S., Carson J. E., 1995, *A&AS*, 114, 197  
 An T. et al., 2012a, *ApJS*, 198, 5  
 An T., Baan W. A., 2012b, *ApJ*, 760, 77  
 Chuprikov A. A. et al., 1999, *NewAR*, 43, 747  
 Croston J. H., Hardcastle M. J., Harris D. E., Belsole E., Birkinshaw M., Worrall D. M., 2005, *ApJ*, 626, 733

Dallacasa D., Fanti C., Fanti R., Schilizzi R. T., Spencer R. E., 1995, *A&A*, 295, 27  
 Dallacasa D., Orienti M., Fanti C., Fanti R., Stanghellini C., 2013, *MNRAS*, 433, 147  
 Douglas J. M., Bash F. N., Bozyan F. A., Torrence G. W., Wolfe C., 1996, *AJ*, 111, 1945  
 Fanti C. et al., 1989, *A&A*, 217, 44  
 Fanti C., Fanti R., Schilizzi R. T., Spencer R. E., van Breugel W. J. M., 1986, *A&A*, 170, 10  
 Fanti R., Fanti C., Schilizzi R. T., Spencer R. E., Nan R., Parma P., van Breugel W. J. M., Venturi T., 1990, *A&A*, 231, 333  
 Fanti C., Fanti R., Dallacasa D., Schilizzi R. T., Spencer R. E., Stanghellini C., 1995, *A&A*, 302, 317  
 Fanti C., Pozzi F., Fanti R. et al., 2000, *A&A*, 358, 499  
 Fanti C., Fanti R., Dallacasa D., McDonald A., Schilizzi R. T., Spencer R. E., 2002, *A&A*, 396, 801  
 Giroletti M., Polatidis A., 2009, *AN*, 330, 193  
 Gugliucci N. E., Taylor G. B., Peck A. B., Giroletti M., 2005, *ApJ*, 622, 136  
 Jeyakumar S., Saikia D. J., Pramesh R. A., Balasubramanian V., 2000, *A&A*, 362, 27  
 Kühr H., Witzel A., Pauliny-Toth I. I. K., Nauber U., 1981, *A&AS*, 45, 367  
 Labiano A., Vermeulen R. C., Barthel P. D., O'Dea C. P., Gallimore J. F., Baum S., de Vries W., 2006, *A&A*, 447, 481  
 Laing R. A., Riley J. M., Longair M. S., 1983, *MNRAS*, 204, 151  
 Lenc E., Garrett M. A., Wucknitz O., Anderson J. M., Tingay S. J., 2008, *ApJ*, 673, 78  
 Lüdke E., Garrington S. T., Spencer R. E., Akujor C. E., Muxlow T. W. B., Sanghera H. S., Fanti C., 1998, *MNRAS*, 299, 467  
 Mantovani F., Rossetti A., Junor W., Saikia D. J., Salter C. J., 2013, *A&A*, 555, 4  
 Morganti R., Fogasy J., Paragi Z., Oosterloo T., Orienti M., 2013, *Science*, 341, 1082  
 Murgia M., 2003, *PASA*, 20, 19  
 Murgia M., Fanti C., Fanti R., Gregorini L., Klein U., Mack K.-H., Vigotti M., 1999, *A&A*, 345, 769  
 Murphy T. et al., 2010, *MNRAS*, 402, 2403  
 Nan R., Schilizzi R. T., Fanti C., Fanti R., 1991, *A&A*, 252, 527  
 O'Dea C. P., 1998, *PASP*, 110, 493  
 O'Dea C. P., Saikia D. J., 2021, *A&ARv*, 29, 3  
 Orienti M., 2016, *AN*, 337, 9  
 Pacholczyk A. G., 1970, *Radio Astrophysics*. Freeman & Co., San Francisco  
 Peacock J. A., Wall J. V., 1981, *MNRAS*, 194, 331  
 Polatidis A. G., Conway J. E., 2003, *PASA*, 20, 69  
 Rampadarath H., Garrett M. A., Polatidis A., 2009, *A&A*, 500, 1327  
 Readhead A. C. S., 1994, *ApJ*, 426, 51  
 Readhead A. C. S., Taylor G. B., Pearson T. J., Wilkinson P. N., 1996, *ApJ*, 460, 634  
 Rengelink R. B., Tang Y., de Bruyn A. G., Miley G. K., Bremer M. N., Röttgering H. J. A., Bremer M. A. R., 1997, *A&AS*, 124, 259  
 Sanghera H. S., Saikia D. J., Lüdke E., Spencer R. E., Foulsham P. A., Akujor C. E., Tzioumis A. K., 1995, *A&A*, 295, 629  
 Siemiginowska A., Cheung C. C., LaMassa S. et al., 2005, *ApJ*, 632, 110  
 Snellen I. A. G., Schilizzi R. T., Miley G. K., de Bruyn A. G., Bremer M. N., Röttgering H. J. A., 2000, *MNRAS*, 319, 445  
 Sobolewska M., Siemiginowska A., Guainazzi M., Hardcastle M., Migliori G., Ostorero L., Stawarz Ł., 2019, *ApJ*, 871, 71  
 Spencer R. E., McDowell J. C., Charlesworth M., Fanti C., Parma P., Peacock J. A., 1989, *MNRAS*, 240, 657  
 Tornaiainen I., Tornikoski M., Lähtenmäki A., Aller M. F., Aller H. D., Mingaliev M. G., 2007, *A&A*, 469, 451  
 van Breugel W., Miley G., Heckman T., 1984, *AJ*, 89, 5  
 van Breugel W. J. M., Fanti C., Fanti R., Stanghellini C., Schilizzi R. T., Spencer R. E., 1992, *A&A*, 256, 56  
 Zovaro H. R. M., Sharp R., Nesvadba N. P. H., Bicknell G. V., Mukherjee D., Wagner A. Y., Groves B., Krishna S., 2019, *MNRAS*, 484, 3393



**APPENDIX: PHYSICAL PARAMETERS**

We computed the minimum total energy,  $E_{\min}$ , the minimum energy density,  $u_{\min}$ , the equipartition pressure  $p_{\text{eq}}$ , and the equipartition magnetic field,  $H_{\text{eq}}$ , using

$$E_{\min} = c_{13} L^{4/7} V^{3/7}, \quad (\text{A1})$$

$$u_{\min} = c_{13} \left( \frac{L}{V} \right)^{4/7}, \quad (\text{A2})$$

$$p_{\text{eq}} = \frac{13}{21} u_{\min}, \quad (\text{A3})$$

$$H_{\text{eq}} = \left( \frac{c_{12} L}{V} \right)^{\frac{2}{7}}, \quad (\text{A4})$$

where  $L$  is the radio luminosity,  $V$  is the volume homogeneously filled with relativistic plasma in which electrons and positrons have identical energy, and  $c_{12}$  and  $c_{13}$  are constants tabulated in Pacholczyk (1970) and depend on the spectral index and the upper and lower

cut-off frequencies. We assumed an average spectral index  $\alpha = 0.7$ , a lower cut-off frequency,  $\nu_1 = 10$  MHz, and an upper cut-off frequency,  $\nu_2 = 100$  GHz. The radio luminosity  $L$  was calculated by

$$L = \frac{4\pi D_L^2}{(1+z)^{1-\alpha}} \int_{\nu_1}^{\nu_2} S(\nu) d\nu, \quad (\text{A5})$$

where  $D_L$  is the luminosity distance and  $z$  is the redshift. We approximated the volume of the source components to a prolate ellipsoid:

$$V = \frac{\pi}{6} \left( \frac{D_L}{(1+z)^2} \right)^3 \theta_{\text{maj}} \theta_{\text{min}}^2, \quad (\text{A6})$$

where  $\theta_{\text{maj}}$  and  $\theta_{\text{min}}$  are the major and minor angular sizes, respectively.

This paper has been typeset from a  $\text{\TeX}/\text{\LaTeX}$  file prepared by the author.